IUCrJ
ISSN 2052-2525
MATERIALS | COMPUTATION

Phase transitions in rutile-related $V_{0.92}O_2$ synthesized at high pressures and temperatures

Andrzej Grzechnik,[a,b]* Václav Petříček,[c] Pascal Reiss,[d] Paul Zakalek,[a] Dmitry Chernyshov[e] and Karen Friese[a]

[a]Jülich Centre for Neutron Science, Research Center Jülich, Jülich, 52425, Germany, [b]Institute of Crystallography, RWTH Aachen University, Aachen, 52066, Germany, [c]Institute of Physics, Academy of Sciences of the Czech Republic, Praha, 162 00, Czech Republic, [d]Quantum Materials Department, Max Planck Institute for Solid State Research, Stuttgart, 70569, Germany, and [e]Swiss-Norwegian Beamlines, European Synchrotron Radiation Facility, Grenoble, 38043, France. *Correspondence e-mail: a.grzechnik@fz-juelich.de

Received 29 July 2025
Accepted 30 November 2025

Edited by X. Zhang, Tsinghua University, China

Keywords: vanadium oxides; extreme conditions; phase transitions; structure–property relationships.

B-IncStrDB reference: tYecoNslA2B

CCDC reference: 2512153

Supporting information: this article has supporting information at www.iucrj.org

Structural phase transitions in metastable rutile-related $V_{0.92}O_2$ synthesized at 10 GPa and 1273 K were studied with single-crystal X-ray diffraction in the temperature range 110–500 K and at pressures up to 9.2 GPa. $V_{0.92}O_2$ starts to decompose at 470 K and atmospheric pressure. When heated to temperatures above about 350 K, the material transforms to an incommensurate phase. The oxygen sublattice is essentially rigid and it is mostly the V atoms that are affected by the modulation. An anharmonic description of the displacement parameters and their corresponding modulation is used for the V atoms to reach satisfactory agreement factors for main and first-order satellite reflections, indicating substantial disorder in the modulated structure. Measurements of electronic transport properties provide evidence that the incommensurate phase is insulating. On compression at room temperature, $V_{0.92}O_2$ reaches the ideal rutile structure at about 5.0 GPa. Both structural and electronic phase transitions are of the first-order character. The results of this work demonstrate that the structural and electronic behaviour of $V_{0.92}O_2$ at extreme conditions is distinctly different from that of stoichiometric VO_2.

1. Introduction

Vanadium dioxide (VO_2) undergoes a first-order metal–insulator phase transition (MIT) from the rutile (phase R, $P4_2/mnm$, $Z = 2$) to the monoclinic (phase $M1$, $P2_1/c$, $Z = 4$) polymorphs at about $T_{MIT} = 341$ K (Qazilbash *et al.*, 2007; Shao *et al.*, 2018; Liu *et al.*, 2020; Pouget, 2021; Xue & Yin, 2022; Joshi *et al.*, 2023). The metallic R phase is built of chains of edge-sharing VO_6 octahedra connected by common corners. The V—V distance of 2.85 Å along the chains is equal to the c lattice parameter. The structure of the insulating $M1$ phase is also made of two VO_6 chains, but with V–V dimers in a zigzag pattern due to displacement of the V atoms from the ideal rutile positions (Longo *et al.*, 1970). The $R \rightarrow M1$ structural instability gives rise to pre-transitional diffuse scattering (Pouget, 2021). MIT, which is an improper ferroelastic phase transition, is associated with a magnetic susceptibility drop (Pouget, 2021) and a change in thermochromic properties (Mamakhel *et al.*, 2022).

Doping with low-valence cations (*e.g.* Al^{3+}, Cr^{3+} and Fe^{3+}) stabilizes two additional insulating polymorphs, which are monoclinic (phase $M2$, $C2/m$, $Z = 8$) and triclinic (phase T, $P\overline{1}$, $Z = 4$). In $M2$, there are alternate short and long distances in the linear V—V chain, while the V atoms are equidistant in the other zigzag V—V chain (Marezio *et al.*, 1972; Ghedira *et al.*, 1977). The distortion in T with respect to $M2$ is mainly due to

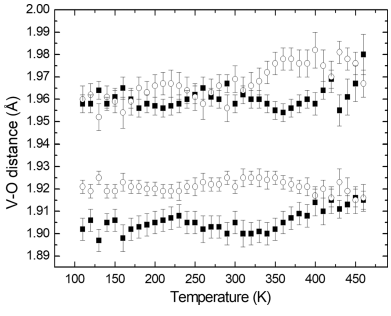

breaking of the linearity and pairing of the V atoms in the zigzag chain (Ghedira *et al.*, 1977). The stabilities of phases *R*, *M*1, *M*2 and *T* are affected by stoichiometry, electric field, strain or pressure (Marezio *et al.*, 1972, Ghedira *et al.*, 1977; Atkin *et al.*, 2012; Liu *et al.*, 2018; Pouget, 2021; Wilson *et al.*, 2022; Bouvier *et al.*, 2023; Joshi *et al.*, 2023). *M*1 and *M*2 can transform into one another, with *T* as an intermediate (Marezio *et al.*, 1972). *M*2 could also be an intermediate in the *M*1→*R* transformation (Liu *et al.*, 2020; Bleu *et al.*, 2023). The three insulating phases may co-exist and form domains (Lu *et al.*, 2014). The high-valence dopants (*e.g.* Nb^{5+}, Mo^{6+} and W^{6+}) lower the T_{MIT}, while the low-valence dopants (*e.g.* Al^{3+}, Cr^{3+} and Fe^{3+}) increase it (Pouget, 2021; Xue & Yin, 2022; Joshi *et al.*, 2023). In the first case, the charge is compensated by the presence of the V^{3+} cations. In the latter, it is compensated by the V^{5+} cations.

^{51}V NMR studies of the metallic and insulating phases of VO_2 provide contradictory results. Boyarsky *et al.* (2000) suggested that MIT is accompanied by the change of the electronic state $2V^{4+} \leftrightarrow V^{3+} + V^{5+}$, with the presence of two structurally and chemically different vanadium cations V^{3+} and V^{5+} in *M*1. On the other hand, the data by Gro Nielsen *et al.* (2002) show the presence of only V^{4+} cations in the insulating phase. Electrical and photoemission investigations by Joshi *et al.* (2023) demonstrated that the V^{3+} and V^{5+} cations co-exist in the metallic state of stoichiometric VO_2 due to charge fluctuations of the V^{4+} cations. The insulating phase is suppressed in VO_{2-x}, while the metallic phase is suppressed in VO_{2+y}. However, Joshi *et al.* (2023) did not present structural data for any of the VO_{2-x} and VO_{2+y} phases across MIT.

The pressure–temperature phase diagram of VO_2 was determined by Chen *et al.* (2017). In addition to the *R* and *M*1 polymorphs, one insulating *M*1′ (monoclinic) phase and two metallic phases *X* (triclinic) and *O* (orthorhombic) were identified. When *M*1 is compressed at room temperature, it transforms to *M*1′ at 13.9 GPa (Bouvier *et al.*, 2023). *X* co-exists with *M*1′ in the pressure range 32–42 GPa. Upon decompression, *X* transforms to another (unidentified) phase between 20 and 3 GPa. The sequence of phase transitions in VO_2 under strong compression was examined by Xie *et al.* (2018).

Apart from VO_2, the experimentally determined equilibrium phases in the central part of the V–O phase diagram (VO_x, $1.5 \leq x \leq 2.5$) at atmospheric pressure are V_2O_3, V_nO_{2n-1} ($n = 3 \div 8$), V_3O_7, V_6O_{13} and V_2O_5 (Wriedt, 1989). The calculated phase diagram for $1.5 \leq x \leq 2.5$ includes only V_2O_3, V_3O_5, VO_2, V_3O_7 and V_2O_5 (Hu *et al.*, 2023). The oxides V_nO_{2n-1} ($n = 3 \div 9$) form a Magnéli homologous series (Schwingenschlögl & Eyert, 2004; Allred & Cava, 2013) according to the formula $V_nO_{2n-1} = V_2O_3 + (n-2)VO_2$. With respect to the composition of vanadium dioxide, they are anion deficient and can also be expressed as VO_{2-y}. The end members of this series are corundum V_2O_3 ($R\bar{3}c$, $Z = 6$) and rutile VO_2 (phase *R*), both with a hexagonal close-packed array of O atoms (Katzke *et al.*, 2003). One oxygen layer is removed at every *n*th vanadium layer in the direction perpendicular to the (211) plane of the parent rutile structure. Magnéli phases are also known for the titanium, niobium and tungsten oxides (Wu *et al.*, 2023).

The homologous series of vanadium oxides V_nO_{2n+1} in the V_2O_5–VO_2 system was predicted by Wadsley (1957). Its formula can be written as $V_nO_{2n+1} = V_2O_5 + (n-2)VO_2$ for $2 \leq n$. With respect to the chemical composition of VO_2, the Wadsley oxides are cation deficient, *i.e.* $V_{1-x}O_2$. The end members of this series are α-V_2O_5 and VO_2(B) (Katzke *et al.*, 2003). These materials have structures derived from VO_x ($Fm\bar{3}m$, $Z = 4$), where $x \simeq 1$, by introducing different ordered vacancies in the oxygen cubic close-packing array. Shear deformations break symmetry and cause the collapse of the face-centred cubic layers along the cubic *c* axis. The cations partially fill out the available voids in the oxygen sublattice in a commensurate way.

Metal-deficient $V_{1-x}O_2$ material, synthesized at 6.5 GPa and 1273 K by substituting V^{5+} into VO_2 (Chamberland, 1973), has a distorted rutile structure ($P2/m$, $Z = 2$), with the V—V distances in both chains equal to the *b* lattice parameter (Galy & Miehe, 1999). Up to 10 wt% of V_2O_5 was accommodated in $V_{1-x}O_2$ at these conditions. Based on the resistivity data, the temperatures for MIT depend on the actual composition (Chamberland, 1973). They increase from 353 to 361 K for 2 wt% ($V_{0.995}O_2$) and 10 wt% of V_2O_5 ($V_{0.976}O_2$), respectively. No structural details of the metallic phase were provided.

Recently, we have grown single crystals of rutile-related $V_{0.92}O_2$ at 10 GPa and 1273 K from a polycrystalline starting material of the Wadsley phase V_6O_{13} (Grzechnik *et al.*, 2024) corresponding in terms of its composition to $V_{1-x}O_2$ (Chamberland, 1973) or VO_{2+y} (Joshi *et al.*, 2023) with 35 wt% of V_2O_5. *In situ* synchrotron measurements revealed that this new phase forms above 500 K in the pressure range 4–17.5 GPa and can be recovered to ambient conditions. The characteristic feature of its crystal structure ($C2/m$, $Z = 4$) is the presence of disorder affecting the V atoms, which occupy the two split-atom positions V1 and V2. The V1 atoms in one of the octahedral chains are displaced along the *b* axis, while the V2 atoms in the other are fourfold split in the *bc* plane. This results in two zigzag V—V chains, one with equidistant V1 atoms and the other with short and long V2—V2 distances. Disregarding the split V-atom positions, the average structure ($P2/m$, $Z = 2$) of this new phase (Fig. 1) is like that for the $V_{1-x}O_2$ material (Chamberland, 1973; Galy & Miehe, 1999). Pseudosymmetry considerations (Grzechnik *et al.*, 2024) indicate that it is the ordered variant of *M*2. The transformation of the Wadsley phase V_6O_{13} into rutile-related $V_{0.92}O_2$ involves the transition from cubic to hexagonal close-packing of the O atoms.

The physical properties of different structural forms of $V_{1-x}O_2$ are closely correlated with the formation and spatial arrangement of the short V—V distances (Liu *et al.*, 2018; Joshi *et al.*, 2023). Detailed experimental characterization of new types of structural ordering, such as the (in)commensurate long- or short-range order, are a necessary step towards the better understanding of structure–property relationships and the further control of the physical properties of vanadium

oxides. While browsing the literature on (non)stoichiometric vanadium dioxides, one can readily see that most of the articles are somewhat incomplete in the sense that either the structural or electronic properties and transformations of $VO_{2\pm x}$ are investigated. In this article, we combine both approaches (i) to determine whether metastable $V_{0.92}O_2$ undergoes any temperature- or pressure-induced phase transitions using single-crystal X-ray diffraction, and (ii) to examine its electronic transport properties at atmospheric pressure for further elucidation of the structure–property relationships in vanadium dioxides.

2. Experimental methods

Single-crystal growth of $V_{0.92}O_2$ from the Wadsley phase V_6O_{13} was described previously (Grzechnik *et al.*, 2024).

Synchrotron single-crystal diffraction measurements (λ = 0.72044 Å) were performed on the BM01 station of the Swiss–Norwegian Beamlines (SNBL) at the European Synchrotron Radiation Facility (Grenoble, France) (Dyadkin *et al.*, 2016). The data (a full rotation of 360°) were collected using a Pilatus 2M detector. After several tests on various crystals at room temperature to check for their quality and for any radiation damage (Grzechnik *et al.*, 2023), our data collection strategy was to measure frames with a fine angular slicing of 0.1° and the exposure time of 0.1 s/frame. The chosen crystal was mounted on a glass pin and placed in the stream of nitrogen from an Oxford Cryostream 700+. It was cooled to 100 K and the data were collected on heating to 500 K with a step of 10 K.

High-pressure single-crystal X-ray data at room temperature were measured on a STOE IPDS-II (Stoe & Cie GmbH, Darmstadt, Germany; λ = 0.71073 Å) equipped with an image plate, as well as on a 4-circle Huber diffractometer with an Ag microfocus Incoatec source (λ = 0.5608 Å) and a Pilatus 300k detector. A crystal of $V_{0.92}O_2$ was loaded into the Ahsbahs diamond anvil cell (Ahsbahs, 2012), together with a 4:1 (*v*/*v*) methanol–ethanol pressure medium and a ruby ball as a pressure marker (Mao *et al.*, 1986).

All the laboratory and synchrotron data collected with the Pilatus detectors were analysed with the program *CrysAlis PRO* (Rigaku Oxford Diffraction, 2024). The data from the IPDS-II diffractometer were processed with the program *X-AREA* (Stoe & Cie, 1998). Solution and refinement of the structures were carried out with the programs *JANA2006* (Petříček *et al.*, 2014) and *JANA2020* (Petříček *et al.*, 2023).

Electronic transport measurements were carried out between 250 and 400 K inside a Quantum Design PPMS system, employing the electrical transport option (ETO). We used a standard four-wire measurement technique with a low AC excitation current of 100 µA to avoid parasitic sample heating and a frequency around 57 Hz. Good electronic contacts were made by attaching 10 µm Au wires to a single crystal of approximate dimensions 0.15 mm × 0.10 mm × 0.08 mm using an Ag paint. We confirmed a negligible phase angle of less than 1° over the temperature range.

3. Results and discussion

3.1. Single-crystal X-ray diffraction in the temperature range 110–500 K and under ambient pressure

On heating from 110 K to about 460 K, all the main reflections in the synchrotron data are indexed and integrated with the primitive monoclinic lattice corresponding to the average structure (*P*2/*m*, *Z* = 2) determined previously (Galy & Miehe, 1999; Grzechnik *et al.*, 2024). Metastable $V_{0.92}O_2$ starts to collapse at above 460 K as the reflections become

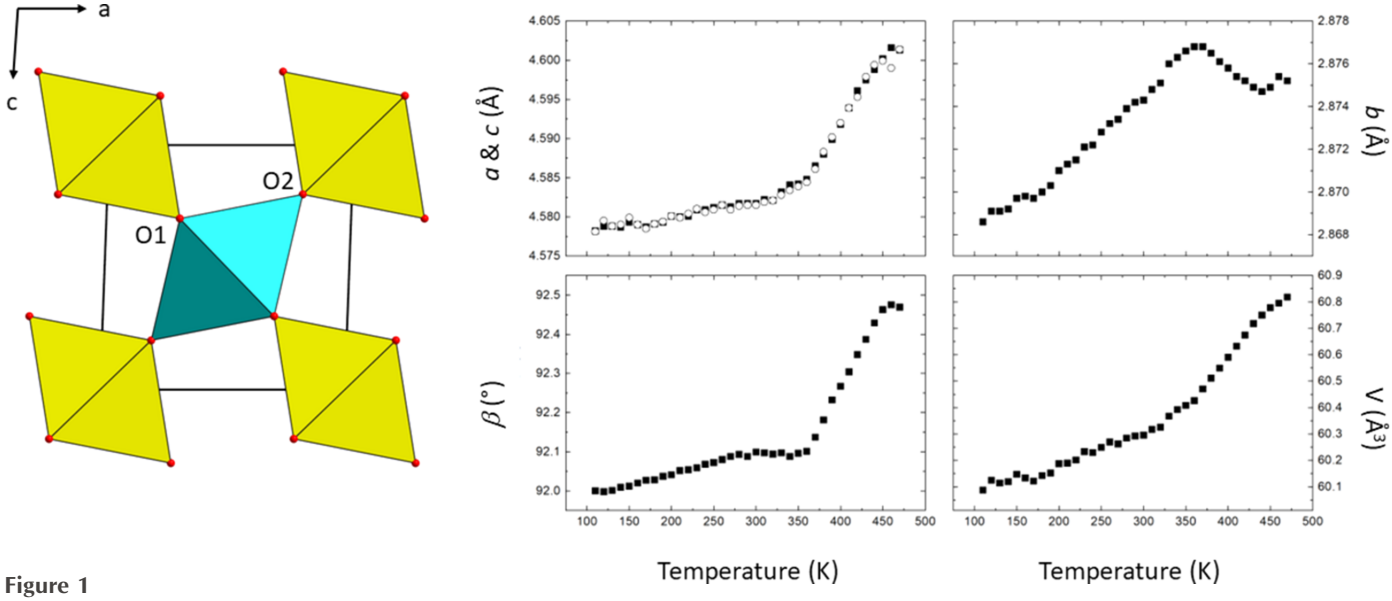

Figure 1
The average crystal structure in the space group *P*2/*m* (*Z* = 2), as well as the temperature dependence of its lattice parameters and unit-cell volumes. The octahedra around the V1 and V2 atoms are drawn in yellow and cyan, respectively. The O1 and O2 atoms are labelled. The symbols in the plots of the lattice parameters and unit-cell volumes are larger than the estimated standard deviations.

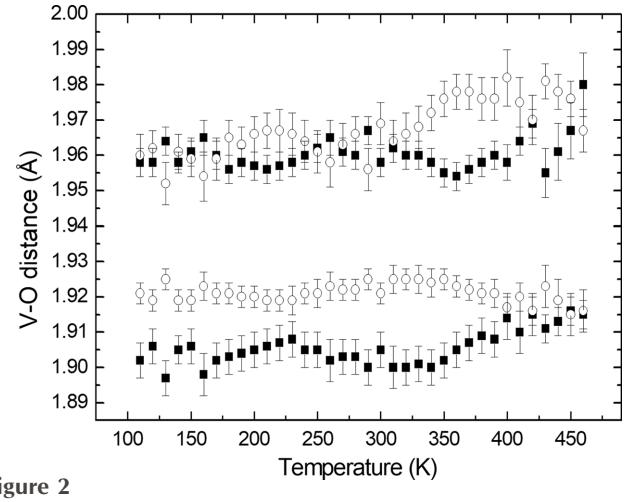

Figure 2
Temperature dependence of the V—O distances in the $V1O_6$ (full symbols) and $V2O_6$ (open symbols) octahedra in the average structure ($P2/m$, $Z = 2$).

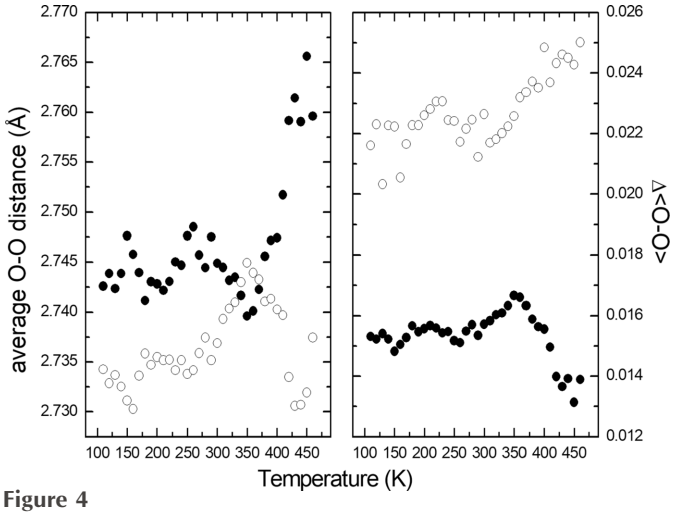

Figure 4
Average O—O distances and $\Delta\langle O-O\rangle$ deviation parameter in the $V1O_6$ (full symbols) and $V2O_6$ (open symbols) octahedra of the average structure ($P2/m$, $Z = 2$). The deviation parameter is defined as $\Delta\langle O-O\rangle = \left(\sum_{i=1}^{12}|OO_i - OO_m|\right)/12OO_m$.

smeared out. Also, new additional reflections appear. Above 470 K, the observed reflections cannot be indexed as originating from a single phase, indicating decomposition of the $V_{0.92}O_2$ material.

From the abrupt changes of the lattice parameters and unit-cell volumes (Fig. 1), it is seen that the material undergoes a first-order iso-symmetrical $P2/m \rightarrow P2/m$ phase transition at about 350 K. The b lattice parameter of the high-temperature phase is smaller than that for the low-temperature phase. The drop in this lattice parameter at the phase transition is correlated with an abrupt shortening of the V—V distances in the octahedral chains. The a and c lattice parameters exhibit the same evolution in the entire temperature range studied here. The β angle, which is a measure of a monoclinic distortion of the tetragonal rutile structure, increases with elevated temperature and has a drastic change of slope at about 350 K. It is remarkable that the temperature of the phase transition

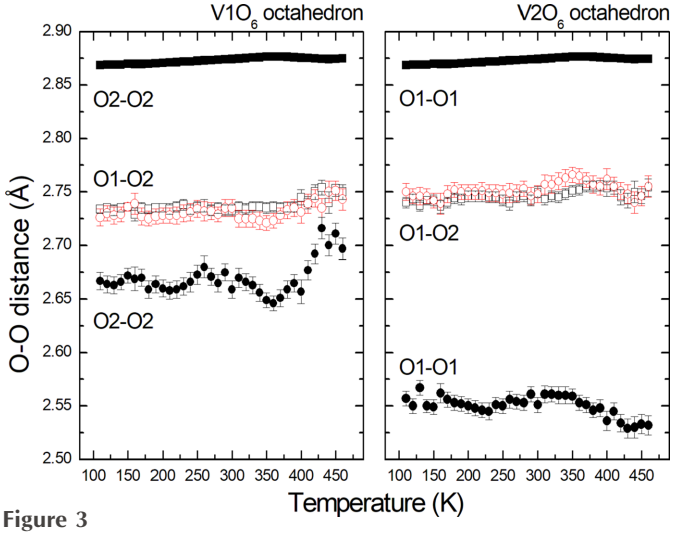

Figure 3
Temperature dependence of the O—O distances in the average structure ($P2/m$, $Z = 2$). The error bars are shown when larger than the symbols.

observed in $V_{0.92}O_2$ is very similar to that observed in $V_{1-x}O_2$, depending on the compositional variable x (Chamberland, 1973; Qazilbash *et al.*, 2007; Liu *et al.*, 2020; Pouget, 2021; Joshi *et al.*, 2023).

The V—O distances in the average structure of $V_{0.92}O_2$ ($P2/m$, $Z = 2$) as a function of temperature are shown in Fig. 2. There is no obvious anomaly that could be associated with the phase transition at about 350 K. However, the O—O distances in both chains of octahedra exhibit clear changes in their temperature dependencies at the phase transition (Fig. 3). The equatorial planes of the octahedra are defined by the atoms involved in edge sharing in the chains. The apical atoms in $V1O_6$ and $V2O_6$ are O1 and O2, respectively. The shortest and longest O—O distances are in the equatorial planes of both polyhedra, *i.e.* the O2—O2 distances in the $V1O_6$ octahedra and the O1—O1 distances in the $V2O_6$ octahedra. The shortest distances correspond to the shared edges of the octahedra. The most affected O—O distances at the phase transition are those in the respective equatorial planes. The average O—O distances abruptly change at the phase transition – they increase in $V1O_6$, while they decrease in $V2O_6$ (Fig. 4). The octahedron around the V1 atom at the site with the higher occupancy is less distorted than that around the V2 atom and becomes more regular above the phase transition.

Diffuse scattering is not observed in the laboratory data measured either on the IPDS-II diffractometer (image plate, Mo $K\alpha$ radiation) or on the 4-circle diffractometer (Pilatus 300k detector, Ag microfocus source). However, the analysis of the reconstructions of the reciprocal space based on the synchrotron measurements reveals the presence of diffuse scattering at all temperatures (Figs. 5 and 6). The intensity of the diffuse scattering increases close to the transition temperature. Above the phase transition, the diffuse features start to condense to well-defined satellite reflections. The strongest diffuse scattering is between the nearest satellites, which could be indexed with one incommensurate wave vector $\mathbf{q} = (\frac{1}{2}, \beta, \frac{1}{2})$,

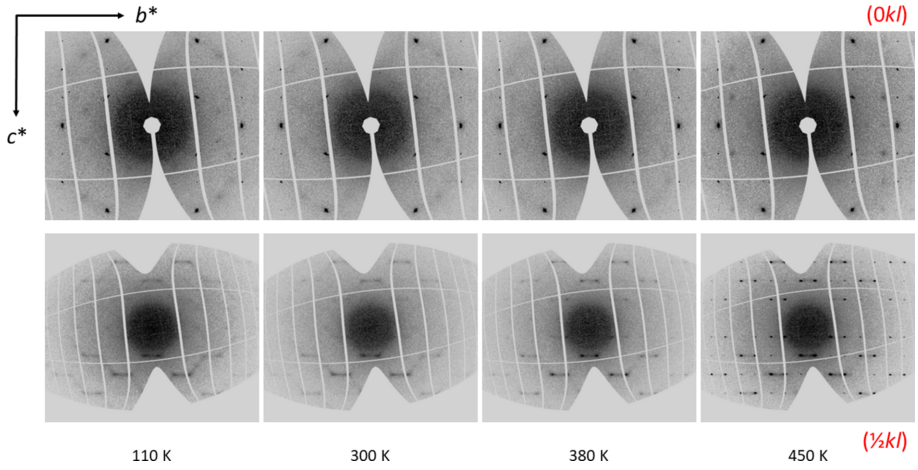

Figure 5
Reconstructions of the reciprocal space in the (0*kl*) and ($\frac{1}{2}$*kl*) planes (the upper and lower row, respectively) from the synchrotron data at selected temperatures.

where $\beta \simeq 0.234$. This vector, which is essentially constant as a function of temperature, can only be precisely determined above 400 K (Fig. 7).[1] All these observations indicate that metastable $V_{0.92}O_2$ does not transform to the ideal rutile structure (*R*) at high temperatures and ambient pressure.

All the main and satellite reflections in the diffraction pattern at 460 K can be indexed and integrated with monoclinic lattice parameters a = 4.5995 (4), b = 2.8746 (2), c = 4.6014 (4) Å and β = 92.49 (1)° in combination with the vector **q** = [$\frac{1}{2}$, 0.2328 (9), $\frac{1}{2}$]. Only first-order satellites were detected. Satellites of the second order do not show any significant intensity in the integration and are also not visible in the reconstructions of reciprocal space. For all the refinements, the overall stoichiometry and occupancies for V1 and V2 were fixed to the values reported by Grzechnik *et al.* (2024), as a free refinement of the occupation parameters showed only minor deviations from this stoichiometry.

The refinement of the average structure at 460 K was carried out in the space groups *P*2/*m*, *P*2, *Pm*, $P\overline{1}$ and *P*1. For the triclinic space groups, additional twinning *via* a twofold axis in the direction [010] was included. For none of the last four space groups were the overall agreement factors significantly better than for *P*2/*m*, considering the higher number of parameters in the refinements.

For the refinements of the incommensurate structure, the structure was transformed according to $a' = a + c$, $b' = b$ and $c' = -a + c$, with a resulting **q** vector of [0, 0.2328 (9), 0] to a pseudo-orthorhombic *X*-centred cell with X = ($\frac{1}{2}$, 0, $\frac{1}{2}$, $\frac{1}{2}$) and an angle of 90.02° (Table 1). Several trial refinements were performed in monoclinic and triclinic superspace groups. Considering the agreement factors and the number of parameters in the refinement, the best result was obtained in superspace group *X*2/*m*(0β0)*s*0. Additional twinning with a twofold axis in the direction [001] was included. The introduction of the twinning led to a significant decrease in the agreement factors for the satellite reflections. In this model, initially only the first harmonics of the Fourier coefficients of a displacive modulation of the V and O atoms were considered. This led to an unsatisfactory *R*(obs) agreement factor of approximately 25% for the satellite reflections and high difference density in the difference Fourier map around the V atoms. When the second harmonic of the displacive modulation function for the V atoms was added, a substantial decrease in the overall agreement factors for the satellite and main reflections was achieved, while introducing higher

Table 1
Experimental and refinement details at 460 K (λ = 0.72044 Å).

Space group	*X*2/*m*(0β0)*s*0
Centring	X = $\frac{1}{2}$, 0, $\frac{1}{2}$, $\frac{1}{2}$
Z	4
a (Å)	6.6458 (6)
b (Å)	2.8746 (2)
c (Å)	6.3631 (6)
β (°)	90.024 (10)
V (Å^3)	121.562 (18)
q vector	0, 0.2328 (9), 0
ρ (g cm^{-3})	4.3091
μ (mm^{-1})	6.934
No. measured reflns	1297
Range of *hkl*	$-8 \le h \le 8$ $-4 \le k \le 4$ $-8 \le l \le 84$ $-1 \le m \le 1$
θ (min/max)	3.53/32.52
No. symmetry independent reflns (all)	445
No. symmetry independent reflns (obs)[a]	302
R_{int}(obs/all)	0.75/0.76
All reflns R(obs)/wR(all)[b]	5.60/7.28
Main reflns R(obs)/wR(all)	5.08/6.44
Satellite reflns R(obs)/wR(all)	9.44/11.74
GoF (obs/all)	5.71/4.44
Twin law	(−100, 0−10, 001)
Twin volumes I/II	0.86 (4)/0.14 (4)
$\Delta\rho_{max}$, $\Delta\rho_{min}$ (e Å^{-3})	0.72, −0.79
No. parameters	92

Symmetry operations: (1) x_1, x_2, x_3, x_4; (2) $-x_1, x_2, -x_3, x_4 + \frac{1}{2}$; (3) $-x_1, -x_2, -x_3, -x_4$; (4) $x_1, -x_2, x_3, -x_4 + \frac{1}{2}$. Notes: (*a*) criterion for the observed reflections is $|F(\text{obs})| > 3\sigma$; (*b*) all agreement factors are given in percent (%) and the weighing scheme is $1/[\sigma^2 F(\text{obs}) + [0.01F(\text{obs})]^2\}$.

[1] The incommensurate vector would be **q** = (0, 0, γ), where $\gamma \approx 0.234$, in the pseudo-orthorhombic *C*-centred cell derived from the primitive monoclinic one using the transformation $a' = a + c$, $b' = -a + c$ and $c' = -b$.

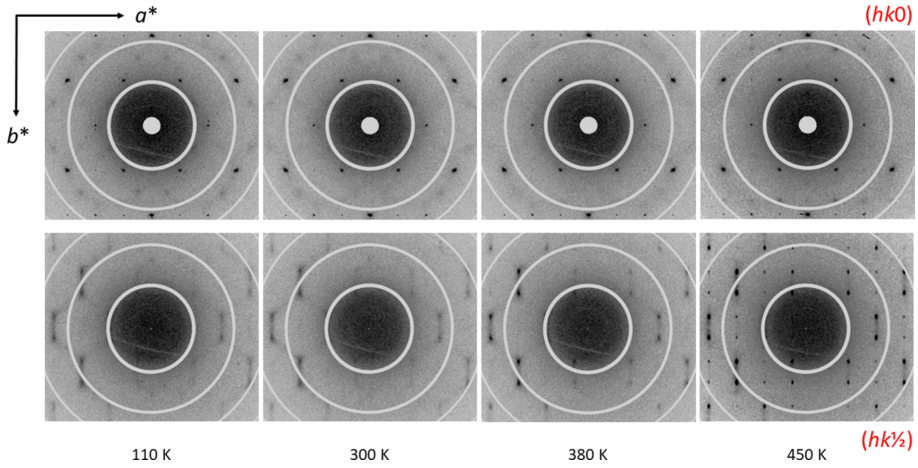

Figure 6
Reconstructions of the reciprocal space in the ($hk0$) and ($hk\frac{1}{2}$) planes (the upper and lower row, respectively) from the synchrotron data at selected temperatures.

harmonics for oxygen or an occupational modulation wave for vanadium did not result in better agreement factors (while leading to an increased data-to-parameter ratio). However, a trial calculation of the intensities of the second-order satellites showed that, assuming this model, their intensities would be substantial so that they should be clearly observed. As this is not the case, it is obvious that this model cannot be the correct one. Also, an inspection of the de Wolff sections and the refined modulation functions around the V-atom positions clearly showed a very bad agreement. We therefore discarded the model with higher harmonics of the displacive modulation.

Instead, we started from the assumption of a modulation of the displacement parameters. The electron density around the V atoms in the average structure (Fig. S1 in the supporting information) was best described using an anharmonic tensor. As the components of the third-order tensor for V are fixed to zero by the symmetry, we introduced a fourth-order anharmonic tensor in the average structure. This led to a substantial decrease in the agreement factors for the main reflections. Introducing a modulation of the anharmonic displacement parameters also led to a significant decrease of the agreement factor for the satellite reflections of first order, while the intensities of the second-order satellites were very small, in accordance with our observations.[2]

According to an earlier chemical analysis, the overall composition of the compound is $V_{0.92}O_2$ (Grzechnik *et al.*, 2024), suggesting vacancies in the V sublattice. However, neither of the de Wolff sections showed any indication of a significant modulation of the height of maxima in the electron density, nor did the introduction and subsequent refinement of occupational modulation lead to better agreement factors. From these observations, we deduced that the V vacancies are randomly distributed within the V sublattice.

In the disordered room-temperature structure, the oxygen sublattice does not substantially deviate from the ideal positions. This observation correlates very well with the fact that the O-atom positions and their displacement parameters are hardly affected by the modulation functions in the incommensurate structure (Table 2). Consequently, the O—O distances do not essentially vary as a function of the internal parameter t if the standard deviations are considered (Table S1 in the supporting information). All these observations imply that the oxygen sublattice is nearly rigid (see animation S1 in the supporting information).

Amplitudes of the displacive modulation of the V atoms are also hardly significant and V—V distances are almost constant in the modulated structure (Table S2). We attribute the absence of significant displacements to the fact that the atoms are disordered over several split atom positions. In our structural model, the anharmonic displacement parameters and their corresponding modulations describe such a disorder of the atoms. While it is thus difficult to quantify the absolute displacements of the V atoms from their average positions, an inspection of the anharmonic displacement parameters reveals that the largest displacements are in the direction of a

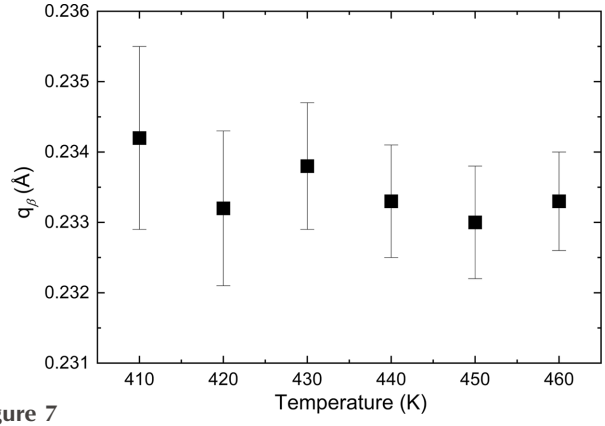

Figure 7
Temperature dependence of the q_β component of the incommensurate vector.

[2] It is noteworthy that part of the elements of the anharmonic tensor and the coefficients of the modulation function of the anharmonic tensor elements refined to values below 3σ. If one restricts these parameters to 0, the overall number of parameters is halved (approximately 40). At the same time, the agreement factors for the satellite reflections increase by approximately 2% [R(obs) = 11.54% and wR(all) = 13.84%].

Table 2
Positional and isotropic displacement parameters of the atoms, as well as Fourier coefficients of the modulation amplitudes at 460 K.

	Occupancy	x	y	z	U_{iso}	
V1	0.492 (4)	0.0	0.0	0.0	0.0318 (11)	
V2	0.428 (4)	0.0	0.5	0.5	0.0283 (13)	
O1	0.5	−0.2003 (2)	0.0	0.5002 (4)	0.0155 (7)	
O2	0.5	0.0005 (3)	0.5	0.2000 (2)	0.0128 (6)	
	$x$sin1	$y$sin1	$z$sin1	$x$cos1	$y$cos1	$z$cos1
V1	0.0065 (4)	0.0	0.0003 (6)	0.0	0.0	0.0
V2	−0.0059 (4)	0.0	0.0001 (6)	0.0	0.0	0.0
O1	−0.0004 (3)	0.0	−0.0004 (6)	0.0	−0.0039 (8)	0.0
O2	0.0008 (3)	0.0	0.0001 (5)	0.0	0.0003 (10)	0.0
	u_{11}	u_{22}	u_{33}	u_{12}	u_{13}	u_{23}
V1	0.0693 (14)	0.0155 (18)	0.010 (2)	0.0	0.0068 (16)	0.0
V2	0.051 (2)	0.027 (2)	0.007 (3)	0.0	0.0025 (18)	0.0
O1	0.0147 (11)	0.0171 (9)	0.0147 (14)	0.0	0.0009 (12)	0.0
O2	0.0186 (13)	0.0112 (8)	0.0085 (12)	0.0	0.0059 (16)	0.0
V1/V2				u_{ij}sin1 = 0.0		
	u_{11}sin1	u_{22}sin1	u_{33}sin1	u_{12}sin1	u_{13}sin1	u_{23}sin1
O1	−0.0009 (11)	−0.0002 (10)	−0.0004 (13)	0.0	0.0012 (15)	0.0
O2	0.0006 (17)	−0.0001 (13)	0.0020 (17)	0.0	−0.0004 (9)	0.0
	u_{11}cos1	u_{22}cos1	u_{33}cos1	u_{12}cos1	u_{13}cos1	u_{23}cos1
V1		For $i = j$ u_{ij}cos1 = 0.0		0.0007 (9)	0.0	0.0012 (14)
V2				−0.0001 (11)	0.0	−0.0004 (16)
O1				0.0012 (7)	0.0	−0.0024 (15)
O2				−0.0008 (7)	0.0.	−0.0005 (12)
	D_{1111}	D_{1113}	D_{1122}	D_{1133}	D_{1223}	D_{1333}
V1	−0.0975 (13)	0.0019 (12)	−0.006 (3)	−0.0009 (8)	−0.005 (3)	−0.0007 (19)
V2	−0.019 (2)	−0.0022 (18)	−0.017 (3)	0.0017 (12)	−0.007 (3)	−0.003 (2)
	D_{2222}	D_{2233}	D_{3333}	$D_{1112} = D_{1123} = D_{1222} = D_{1233} = D_{2223} = D_{2333} = 0.0$		
V1	0.07 (4)	−0.009 (3)	0.000 (3)			
V2	−0.10 (4)	−0.012 (3)	−0.002 (3)			
	C_{111}sin1	C_{113}sin1	C_{122}sin1	C_{133}sin1	C_{223}sin1	C_{333}sin1
V1	−0.048 (2)	0.006 (2)	−0.015 (4)	−0.0037 (13)	−0.000 (5)	0.002 (3)
V2	0.022 (3)	−0.004 (2)	0.016 (5)	0.0020 (12)	0.000 (6)	0.000 (4)
V1/V2			C_{112}sin1 = C_{123}sin1 = C_{222}sin1 = C_{233}sin1 = 0.0			
V1/V2			C_{ijk}cos1 = 0.0			
	D_{1112}cos1	D_{1123}cos1	D_{1222}cos1	D_{1233}cos1	D_{2223}cos1	D_{2333}cos1
V1	−0.000 (3)	0.002 (2)	0.008 (9)	−0.0002 (12)	0.007 (11)	−0.000 (4)
V2	0.006 (3)	−0.002 (3)	−0.004 (10)	0.0004 (15)	0.005 (13)	−0.002 (4)
V1/V2	D_{1111}cos1 = D_{1113}cos1 = D_{1122}cos1 = D_{1133}cos1 = D_{1223}cos1 = D_{1333}cos1 = D_{2222}cos1 = D_{2233}cos1 = D_{3333}cos1 = 0.0					
V1/V2	D_{ijkl}sin1 = 0.0					

(animation S1). This is also clearly visible in animations S2 and S3, which show the joint probability density function (j.p.d.f.) around the V-atom positions in the modulated structure. Animations S4 and S5 show the j.p.d.f. around the O atoms. A complete animation of the incommensurate phase, including the j.p.d.f. for all the atoms in the unit cell, is in animation S6.

In the disordered room-temperature structure, the V1 atoms are arranged in a zigzag pattern, with a V1—V1 distance of 2.9020 (2) Å. In the modulated structure, the average V1—V1 and V2—V2 distances are slightly smaller at 2.87489 (3) and 2.87484 (3) Å, respectively. Thus, surprisingly, the V—V distances are smaller at higher temperatures. However, the true positions of vanadium in the modulated structure are difficult to determine due to the additional disorder modelled by the anharmonic displacement parameters and their modulation.

Considering the $V1O_6$ octahedra, in the modulated structures there are four shorter V—O bonds, plus two longer ones (Table S3). On the other hand, within the $V2O_6$ octahedra, the situation is reversed and there are four longer and two shorter V—O bonds (Table S3).

In the disordered structure at room temperature, the bond valence sums (BVSs) of V1 and V2 are basically equal and amount to about 4.0 v.u. (with the BVS parameters for V^{4+}) or about 4.4 v.u. (with the BVS parameters for V^{5+}). In the modulated structure, the bond valence sums are smaller, with values of around 3.80 for both V atoms assuming a bond valence parameter of V^{4+} and 4.15 for a bond-valence para-

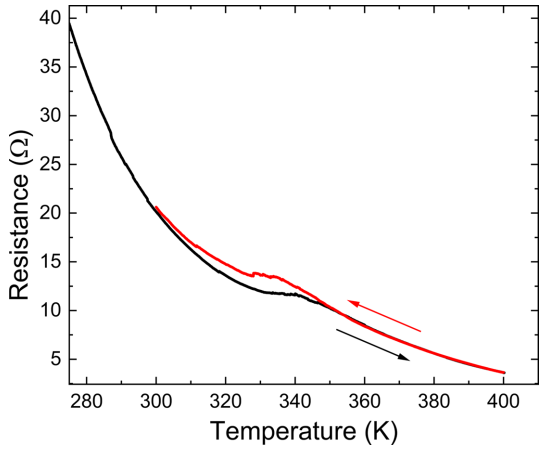

Figure 8
Resistance *versus* temperature on heating (black line) and cooling (red line) in the range 275–400 K.

meter of V^{5+}. Again, one must consider that these parameters are based on the average V-atom coordinates and do not really reflect the deviations from these average positions described by the anharmonic parameters.

3.2. Measurements of electronic transport properties at atmospheric pressure

Fig. 8 shows qualitatively the evolution of resistance measured on a single crystal of $V_{0.92}O_2$ on heating and cooling in the range 275–400 K. The onset of a first-order phase transition is at about 330 K. A hysteresis of about 10 K is observed on cooling the crystal from 400 K to room temperature. The data clearly show that both phases are non-metallic. $V_{0.92}O_2$ becomes even more insulating above the phase transition. Such a behaviour is different from that of (nearly) stoichiometric VO_2, in which the high-temperature phases are metallic (Chamberland, 1973; Joshi *et al.*, 2023).

3.3. Single-crystal X-ray diffraction to 9.2 GPa at room temperature

The high-pressure single-crystal data measured on both laboratory diffractometers up to 9.2 GPa at room temperature were analyzed in the average structure in $P2/m$ ($Z = 2$). The β angle decreases on compression, and it becomes equal to 90° at 4.9 GPa (Fig. 9). All the reflections at this and higher pressures can be indexed with the tetragonal lattice: $a \simeq 4.5$ Å and $c \simeq 2.8$ Å. There is also a discontinuity in the lattice parameters $b_m \leftrightarrow c_t$, which are determined by the V—V distances in the octahedral chains. This implies a first-order phase transition from the monoclinic to tetragonal phases at about 3.7–4.9 GPa. The data measured at 6.35 GPa and room temperature on the 4-circle diffractometer could be integrated and refined with the ideal rutile structure (Tables S4–S6). The $P2/m \leftrightarrow P4_2/mnm$ phase transition is reversible on decompression. All these observations agree with our previous observations about the fact that, on quenching to ambient conditions, rutile $V_{0.92}O_2$ transforms to a range of its distorted variants depending on the actual highest pressure and temperature reached during the synthesis (Grzechnik *et al.*, 2024). The behaviour of metal-deficient $V_{0.92}O_2$ at high pressures

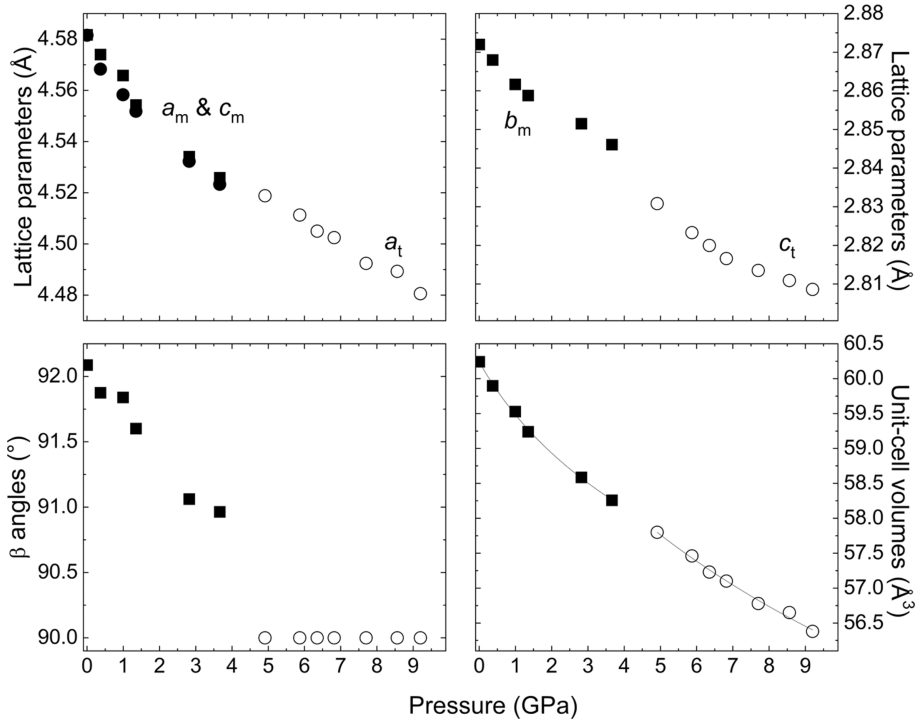

Figure 9
Lattice parameters, β angles and unit-cell volumes for the monoclinic (m, full symbols) and tetragonal (t, open symbols) phases on compression at room temperature. The estimated standard deviations are smaller than the size of the symbols. The solid lines are the fits of the third-order Murnaghan equations of state.

and room temperature is therefore different from that of the *M*1 phase of stoichiometric VO_2, which transforms to a series of low-symmetry polymorphs but not to ideal rutile (Chen *et al.*, 2017; Bouvier *et al.*, 2023).

The monoclinic phase is much more compressible than the tetragonal one. The *P*–*V* data up to 3.66 GPa can be fitted with the third-order Murnaghan equation of state (EoS): V_0 = 60.24 (2) Å^3, B_0 = 66 (3) GPa and B_0' = 29 (3). Since the zero-pressure volume V_0 for the tetragonal polymorph cannot be determined from the EoS fit, a modified third-order Murnaghan EoS in terms of $(P - P_{tr})$, where P_{tr} = 4.91 GPa in the transition pressure, was used. Consequently, V_{tr} = 57.80 (2) Å^3, B_{tr} = 143 (13) GPa and B_{tr}' = 16 (8) are obtained at P_{tr} = 4.91 GPa. The B_0/B_{tr} and B_0'/B_{tr}' parameters can be compared with those for the different polymorphs of stoichiometric VO_2. The bulk modulus B_0 for the phase *M*1 determined theoretically (Dong & Liu, 2013) is 237 GPa, while the reported experimental values are 213 (2) (Bai *et al.*, 2015) and 194 (7) GPa (Bouvier *et al.*, 2023). The theoretical B_0 for *M*2 is 241 GPa (Dong & Liu, 2013). According to the calculations by Dong & Liu (2013), B_0 for rutile VO_2 is 243 GPa. The experimental B_0 for rutile at 383 K is 190 (2) GPa (Bai *et al.*, 2015). The most compressible polymorph of stoichiometric vanadium dioxide is VO_2(B), with B_0 = 129 (4) GPa (Wang *et al.*, 2016), which is comparable to $V_{0.92}O_2$. The first derivatives of the bulk moduli for $V_{0.92}O_2$ are higher than all those for VO_2, which are in the range 4–7 (Dong & Liu, 2013; Bai *et al.*, 2015; Wang *et al.*, 2016; Bouvier *et al.*, 2023).

4. Conclusions

Structural modulations are usually stabilized at low temperatures as a disordered structure transforms into a more ordered one on cooling. Notable exceptions are brownmillerites $Ca_2Fe_2O_5$ (Krüger *et al.*, 2005) and $Ca_2Al_2O_5$ (Lazic *et al.*, 2008), as well as intermetallic PdBi (Folkers *et al.*, 2020). In the brownmillerites at about 1000 K, the modulation arises from the incommensurate sequence of enantiomorphic left- and right-handed tetrahedral BO_4 chains (*B* = Fe or Al). In PdBi with the structure related to TlI, the incommensurability on heating to above 473 K originates from the presence of nearly regular TlI-type slabs in a distorted TlI superstructure with Pd–Pd dimers. Folkers *et al.* (2020) interpreted the TlI-type slabs as the regions of higher vibrational freedom that are entropically favoured at high temperatures. Metastable $V_{0.92}O_2$, which is investigated in this study, undergoes a phase transition to an incommensurate phase above about 350 K. Our interpretation is that such behaviour is a consequence of an incommensurate way of disordering of V^{4+} and V^{5+} cations, which are chemically and structurally distinct with different ionic radii, in a rigid hexagonal close-packing oxygen sublattice. Eventually, $V_{0.92}O_2$ starts to decompose above 460 K at atmospheric pressure. In other words, decomposition is preceded by incommensurability. Such a phenomenon could possibly be found in other materials, not necessarily metastable and synthesized at high pressures.

$V_{0.92}O_2$, which contains 35 wt% of V_2O_5, is insulating. It demonstrates the capacity of the rutile-type framework to accommodate a wide series of VO_2–V_2O_5 compositions. It also suggests that by varying stoichiometries and pressure–temperature conditions one would synthesize rutile-related $V_{1-x}O_2$ materials with transport properties ranging from metallic to insulating. Since the compound with 10 wt% of V_2O_5 ($V_{0.976}O_2$) is indeed metallic (Chamberland, 1973), it remains to be seen for which higher V_2O_5 contents $V_{1-x}O_2$ oxides become insulating. In addition, 35 wt% of V_2O_5 does not need to be a compositional limit for the stability of the rutile-related structure that has one important feature common to all the known (non-)stochiometric VO_2 phases: the hexagonal close-packing oxygen sublattice is rigid, while the cation sublattice is flexible, allowing for various schemes of cation (dis)order. Therefore, incommensurate phases could also be expected for other $V_{1-x}O_2$ compositions, apart from $V_{0.92}O_2$.

Metal-deficient $V_{0.92}O_2$ reversibly transforms to the ideal rutile structure ($P4_2/mnm$, Z = 2) at about 5 GPa and room temperature. Altogether, the results of this work demonstrate that its structural behaviour under extreme conditions is distinctly different from that of stoichiometric VO_2.

Our findings imply then that the structural and electronic (in)stabilities of the non-stoichiometric vanadium dioxides warrant detailed investigations since the occurrence of the metallic *R* phases ($P4_2/mnm$, Z = 2) in the mixed-valence $VO_{2\pm x}$ materials for different $x \neq 0$ is not certain. As our work was focused on Bragg diffraction, further insight into the mechanism of the unusual phase transition observed in $V_{0.92}O_2$ on increasing the temperature could be obtained by a future detailed investigation of the diffuse scattering, which seems to occur as a precursor effect to the formation of the modulated structure.

Acknowledgements

Charlie McMonagle assisted us with setting up the low-temperature measurements at the SNBL. We thank Micha Hölzle, Fabian Beule, Robert Swaczyna and Roman Schäfer for their help with configuring our laboratory 4-circle diffractometer. This work was supported by the Helmholtz InnoPool Project MATHIPE (MATerials under HIgh PrEssure). Crystallography at the Institute of Physics was supported by MGML (mgml.eu) as part of the Czech Research Infrastructures program (project no. LM2023065).

Conflict of interest

There are no conflicts of interest.

Data availability

The data supporting the results reported here can be accessed within the article and supporting information.

References

Ahsbahs, H. (2012). *Z. Kristallogr.* **219**, 305.
Allred, J. M. & Cava, R. J. (2013). *J. Solid State Chem.* **198**, 10–17.

Atkin, J. M., Berweger, S., Chavez, E. K., Raschke, M. B., Cao, J., Fan, W. & Wu, J. (2012). *Phys. Rev. B* **85**, 020101.
Bai, L., Li, Q., Corr, S. A., Meng, Y., Park, C., Sinogeikin, S. V., Ko, C., Wu, J. & Shen, G. (2015). *Phys. Rev. B* **91**, 104110.
Bleu, Y., Bourquard, F., Misdanitis, K., Poulet, A., Loir, A.-S., Garrelie, F. & Donnet, C. (2023). *Mater. Today Commun.* **35**, 105564.
Bouvier, P., Bussmann, L., Machon, D., Breslavetz, I., Garbarino, G., Strobel, P. & Dmitriev, V. (2023). *Phys. Rev. B* **108**, 144106.
Boyarsky, L. A., Gabuda, S. P. & Kozlova, S. G. (2000). *Physica B* **284–288**, 1454–1455.
Chamberland, B. L. (1973). *J. Solid State Chem.* **7**, 377–384.
Chen, Y., Zhang, S., Ke, F., Ko, C., Lee, S., Liu, K., Chen, B., Ager, J. W., Jeanloz, R., Eyert, V. & Wu, J. (2017). *Nano Lett.* **17**, 2512–2516.
Dong, H. & Liu, H. (2013). *Solid State Commun.* **167**, 1–4.
Dyadkin, V., Pattison, P., Dmitriev, V. & Chernyshov, D. (2016). *J. Synchrotron Rad.* **23**, 825–829.
Folkers, L. C., Mitchell Warden, H. E., Fredrickson, D. C. & Lidin, S. (2020). *Inorg. Chem.* **59**, 4936–4949.
Galy, J. & Miehe, G. (1999). *Solid State Sci.* **1**, 433–448.
Ghedira, G., Vincent, H., Marezio, M. & Launay, J. C. (1977). *J. Solid State Chem.* **22**, 423–438.
Gro Nielsen, U., Skibsted, J. & Jakobsen, H. J. (2002). *Chem. Phys. Lett.* **356**, 73–78.
Grzechnik, A., Hakala, B. V., Kurig, S., Walte, N., Tsujino, N., Kakizawa, S., Higo, Y., Zagorac, D., Zagorac, J., Dronskowski, R., Schön, J. C. & Friese, K. (2024). *Cryst. Growth Des.* **24**, 5582–5592.
Grzechnik, A., Petříček, V., Chernyshov, D., McMonagle, C., Geise, T., Shahed, H. & Friese, K. (2023). *Acta Cryst. B* **79**, 103–113.
Hu, P., Hu, P., Vu, T. D., Li, M., Wang, S., Ke, Y., Zeng, X., Mai, L. & Long, Y. (2023). *Chem. Rev.* **123**, 4353–4415.
Joshi, S., Smieszek, N. & Chakrapani, V. (2023). *Sci. Rep.* **10**, 17121.
Katzke, H., Tolédano, P. & Depmeier, W. (2003). *Phys. Rev. B* **68**, 024109.
Krüger, H. & Kahlenberg, V. (2005). *Acta Cryst.* B**61**, 656–662.
Lazic, B., Krüger, H., Kahlenberg, V., Konzett, J. & Kaindl, R. (2008). *Acta Cryst.* B**64**, 417–425.
Liu, K., Lee, S., Yang, S., Delaire, O. & Wu, J. (2018). *Mater. Today* **21**, 875–896.
Liu, M., Xie, S., Wei, L., Galluzzi, M., Li, Y., Wang, Q., Zhou, X., Wang, Y. & Li, J. (2020). *Acta Mater.* **195**, 720–727.
Longo, J. M., Kierkegaard, P., Ballhausen, C. J., Ragnarsson, U., Rasmussen, S. E., Sunde, E. & Sørensen, N. A. (1970). *Acta Chem. Scand.* **24**, 420–426.
Lu, P., Zhou, J., Liu, X., Zhang, Z., Xu, F., Zhang, L., Mou, X., Feng, J., Gao, Y. & Zhao, J. (2014). *J. Appl. Cryst.* **47**, 732–738.
Mamakhel, A., Gjørup, F. H., Kløve, M., Borup, K. & Iversen, B. B. (2022). *Inorg. Chem.* **61**, 8760–8766.
Mao, H. K., Xu, J. & Bell, P. M. (1986). *J. Geophys. Res.* **91**, 4673–4676.
Marezio, M., McWhan, D. B., Remeika, J. P. & Dernier, P. D. (1972). *Phys. Rev. B* **5**, 2541–2551.
Petříček, V., Dušek, M. & Palatinus, L. (2014). *Z. Kristallogr.* **229**, 345–352.
Petříček, V., Palatinus, L., Plášil, J. & Dušek, M. (2023). *Z. Kristallogr.* **238**, 271–282.
Pouget, J.-P. (2021). *C. R. Phys.* **22**, 37–87.
Qazilbash, M. M., Brehm, M., Chae, B.-G., Ho, P.-C., Andreev, G. O., Kim, B.-J., Yun, S. J., Balatsky, A. V., Maple, M. B., Keilmann, F., Kim, H.-T. & Basov, D. N. (2007). *Science* **318**, 1750–1753.
Rigaku Oxford Diffraction (2024). *CrysAlis PRO*. Rigaku Oxford Diffraction Ltd, Yarnton, Oxfordshire, England.
Schwingenschlögl, U. & Eyert, V. (2004). *Ann. Phys.* **13**, 475–510.
Shao, Z., Cao, X., Luo, H. & Jin, P. (2018). *NPG Asia Mater.* **10**, 581–605.
Stoe & Cie (1998). *X-AREA*. Stoe & Cie GmbH, Darmstadt, Germany.
Wadsley, A. D. (1957). *Acta Cryst.* **10**, 261–267.
Wang, Y., Zhu, J., Yang, W., Wen, T., Pravica, M., Liu, Z., Hou, M., Fei, Y., Kang, L., Lin, Z., Jin, C. & Zhao, Y. (2016). *Nat. Commun.* **7**, 12214.
Wilson, C. E., Gibson, A. E., Cuillier, P. M., Li, C.-H., Crosby, P. H. N., Trigg, E. B., Najmr, S., Murray, C. B., Jinschek, J. R. & Doan-Nguyen, V. (2022). *Sci. Rep.* **12**, 14767.
Wriedt, H. A. (1989). *Bull. Alloy Phase Diagrams* **10**, 271–277.
Wu, X., Wang, H. & Wang, Y. (2023). *Materials* **16**, 6874.
Xie, S.-Y., Wang, L., Liu, F., Li, X.-B., Bai, L., Prakapenka, V. B., Cai, Z., Mao, H.-K., Zhang, S. & Liu, H. (2018). *J. Phys. Chem. Lett.* **9**, 2388–2393.
Xue, Y. & Yin, S. (2022). *Nanoscale* **14**, 11054–11097.